IOP Publishing Journal of Physics D: Applied Physics

J. Phys. D: Appl. Phys. **46** (2013) 245202 (12pp) doi:10.1088/0022-3727/46/24/245202

Transport control of dust particles via the electrical asymmetry effect: experiment, simulation and modelling

Shinya Iwashita[1], Edmund Schüngel[1], Julian Schulze[1], Peter Hartmann[2], Zoltán Donkó[2], Giichiro Uchida[3], Kazunori Koga[3], Masaharu Shiratani[3] and Uwe Czarnetzki[1]

[1] Institute for Plasma and Atomic Physics, Ruhr University Bochum, 44780 Bochum, Germany
[2] Institute for Solid State Physics and Optics, Wigner Research Centre for Physics, Hungarian Academy of Sciences, H-1525 Budapest POB 49, Hungary
[3] Department of Electronics, Kyushu University, 819-0395 Fukuoka, Japan

E-mail: shinya.iwashita@rub.de

Received 19 November 2012, in final form 2 May 2013
Published 3 June 2013
Online at stacks.iop.org/JPhysD/46/245202

Abstract
The control of the spatial distribution of micrometre-sized dust particles in capacitively coupled radio frequency discharges is relevant for research and applications. Typically, dust particles in plasmas form a layer located at the sheath edge adjacent to the bottom electrode. Here, a method of manipulating this distribution by the application of a specific excitation waveform, i.e. two consecutive harmonics, is discussed. Tuning the phase angle θ between the two harmonics allows one to adjust the discharge symmetry via the electrical asymmetry effect (EAE). An adiabatic (continuous) phase shift leaves the dust particles at an equilibrium position close to the lower sheath edge. Their levitation can be correlated with the electric field profile. By applying an abrupt phase shift the dust particles are transported between both sheaths through the plasma bulk and partially reside at an equilibrium position close to the upper sheath edge. Hence, the potential profile in the bulk region is probed by the dust particles providing indirect information on plasma properties. The respective motion is understood by an analytical model, showing both the limitations and possible ways of optimizing this sheath-to-sheath transport. A classification of the transport depending on the change in the dc self-bias is provided, and the pressure dependence is discussed.

(Some figures may appear in colour only in the online journal)

1. Introduction

Dusty plasmas exhibit interesting physical phenomena [1, 2] such as the interaction of the plasma sheath [3–6] and bulk [7] with the dust particles, the occurrence of waves [8] and instabilities [9–11], phase transitions [12–16], and the formation of Coulomb crystals [17–20]. They have drawn great attention for industrial application because dust particles in plasmas play various roles: on the one hand the accumulation of dust particles is a major problem for device operation in fusion plasma reactors as well as for semiconductor manufacturing [21–25], i.e. they are impurities to be removed. On the other hand, they are of general importance for deposition purposes [26, 27] and it is well known that an enhanced control of such dust particles in plasmas has the potential to realize the bottom up approach of fabricating novel materials, e.g. microelectronic circuits, medical components, and catalysts [28–33]. In all cases the manipulation of dust particles, which is realized by controlling forces exerted on them such as electrostatic, thermophoretic, ion drag, and gravitational forces, or externally applied ones, e.g. created by a laser beam [34–37], is crucially important. Furthermore, the use of dust particles as probes of these forces revealing plasma properties is a current topic of research [38, 39].

We have developed a novel method to control the transport of dust particles in a capacitively coupled radio frequency (CCRF) discharge by controlling the electrical symmetry of the discharge [40]. Alternative dust manipulation methods

 © 2013 IOP Publishing Ltd Printed in the UK & the USA

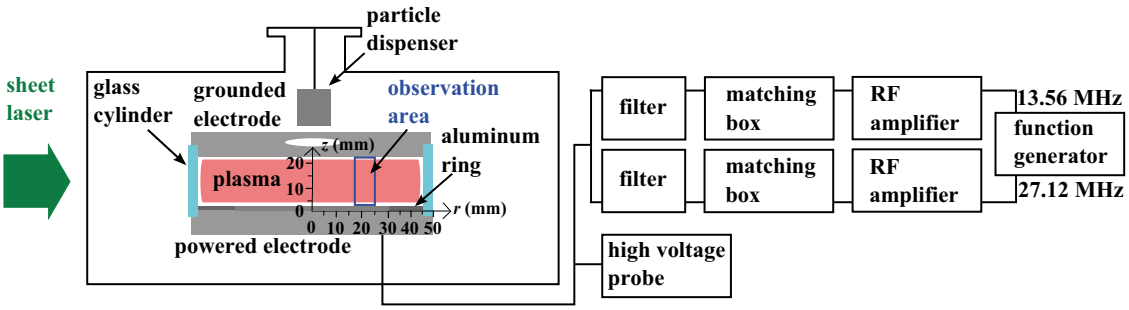

Figure 1. Sketch of the experimental setup.

using electrical pulses applied to wires have also been reported [41–44]. Our dust manipulation method is based on the electrical asymmetry effect (EAE) [45]. The EAE allows one to generate and control a dc self-bias, η, electrically even in geometrically symmetric discharges. It is based on driving one electrode with a particular voltage waveform, $\phi_{\sim}(t)$, which is the sum of two consecutive harmonics with an adjustable phase shift, θ:

$$\phi_{\sim}(t) = \tfrac{1}{2}\phi_0[\cos(2\pi f t + \theta) + \cos(4\pi f t)]. \qquad (1)$$

Here, ϕ_0 is the identical amplitude of both harmonics. In such discharges, η is an almost linear function of θ. In this way, separate control of the ion mean energy and flux at both electrodes is realized in an almost ideal way. At low pressures of a few Pa, the EAE additionally allows one to control the maximum sheath voltage and width at each electrode by adjusting θ [45], resulting in the control of forces exerted on dust particles, such as electrostatic and ion drag forces. In contrast to the pulsing methods mentioned above, the change in the phase angle does not require a change in the applied power or RF amplitude. Furthermore, it is a radio frequency technique, i.e. no dc voltage is applied externally and the EAE is, therefore, applicable to capacitive discharge applications with dielectric electrode surfaces, without the need for additional electrodes or power supplies for pulsing. The EAE can be optimized with respect to the control range of the dc self-bias by choosing non-equal voltage amplitudes for the individual harmonics [46] or by adding more consecutive harmonics to the applied voltage waveform [47, 48]. In this study we intend to describe the basic mechanisms of the manipulation of the dust particle distribution in electrically asymmetric CCRF discharges. Thus, we restrict ourselves to the simplest case described by equation (1). It is important for the analysis carried out in this work that the dust density is sufficiently low so that the plasma parameters are not disturbed by the dust particles. A large concentration of dust particles disturbs the electron density and can cause a significant change of the dc self-bias when distributed asymmetrically between the sheaths [49–51]. The critical parameter for the disturbance is Havnes' value: $P = 695 T_e r_d n_d / n_i$, where T_e, r_d, n_d and n_i are electron temperature, radius of dust particles, their number density and ion density, respectively [17, 52]. P is basically the ratio of the charge density of dust particles to that of ions. The concentration of dust particles disturbs the electron density for $P > 1$, while it does not for $P \ll 1$. In the critical region $P_c = 0.1$–1 the charge of the dust particles becomes significant in the total charge balance [52]. We calculate $P \approx 10^{-3}$ for our experiment, which is well below the P_c. For this estimation, direct images of dust particles were analysed and a mean distance between particles of about 1 mm is determined. Thus, the concentration of dust particles is quite low in this study and they do not disturb the plasma.

This paper is structured in the following way: this introduction is followed by a description of the methods used in this work. There, information on the experimental setup as well as the numerical simulation method is provided, and the analytical approaches on the RF sheath driven by non-sinusoidal voltage waveforms and the motion of dust particles in the plasma bulk region are explained. The results, which are presented and discussed in the third section, include the control of the dc self-bias in dusty plasmas via the EAE, the change of the dust levitation position when changing the phase angle adiabatically (continuously), the motion of dust particles through the plasma bulk when tuning the phase angle abruptly, and a classification of the dust particle transport depending on the change in the dc self-bias and the discharge conditions. Finally, concluding remarks are given in section 4.

2. Methods

2.1. Experiment

Figure 1 shows the experimental setup. The experiments are carried out using a CCRF discharge operated in argon gas at $p = 2$–13 Pa, excited by applying $\phi_{\sim}(t)$ according to equation (1) with $f = 13.56$ MHz and $\phi_0 = 200$–240 V. The applied voltage and the dc self-bias are measured using a high-voltage probe. Details of the electrical circuit have been provided in previous papers [40, 53]. The lower (powered) and upper (grounded) electrodes of 100 mm diameter are placed at a distance of $d = 22$ mm. The plasma is confined radially between the electrodes by a glass cylinder to improve the discharge symmetry. Both the grounded chamber and the powered electrode are water cooled to eliminate the influence of the thermophoretic force. The upper electrode has a 20 mm diameter hole sealed with a fine sieve at the centre for injecting SiO_2 dust particles of 1.5 μm in size, from a dispenser situated above the upper electrode. The gap between the upper electrode and the dispenser, which is located at the centre of the upper electrode, is sealed with a teflon ring to prevent any disturbances due to gas flowing through the gap. The supply

of argon gas inside the glass cylinder is realized through slits of a teflon ring, which is placed between the glass cylinder and the grounded electrode. An aluminum ring (100 mm outer diameter, 60 mm inner diameter, 2 mm height) is set on the lower electrode to confine the dust particles radially. The injected dust particles initially tend to reside relatively near the edge inside the aluminum ring, therefore the observation area is taken to be in the region of 2 mm $\leqslant z \leqslant$ 22 mm and 18 mm $\leqslant r \leqslant$ 25 mm using a two-dimensional laser light scattering (2DLLS) method [23, 28, 29, 54] as shown in figure 1. A vertical laser sheet passes between the two electrodes, with height and width of 20 mm and 1 mm, respectively. The laser power is 150 mW at 532 nm. The light scattered by the dust particles is detected through a side window using a CCD camera equipped with an interference filter and running at a frame rate of 30 pictures per second.

2.2. PIC/MCC simulation

The rf discharge is described by a simulation code based on the particle-in-cell approach combined with Monte Carlo treatment of collision processes, PIC/MCC [55–57]. The code is one-dimensional in space and three-dimensional in velocity space. The simulations are performed in pure argon, although PIC/MCC simulations of dusty plasmas have already been reported [58–60]. Our approximation is based on the assumption that the dust particles represent only a minor perturbation to the plasma, which is justified for low concentration of dust particles as is the case in this study. It has been proven that the simulations can be used to explain the motion of dust particles qualitatively as described in [40], and the forthcoming analysis also shows the applicability. The PIC/MCC simulations are performed at pressures between 4 and 12 Pa. Although our simulations are not capable of accounting for any two-dimensional effects, the simulation data are helpful to understand the experimental findings, which are analysed in the direction perpendicular to the electrode surfaces only. In the simulations the discharge is driven by a voltage specified by equation (1). Electrons are reflected from the electrode surfaces with a probability of 0.2 and the secondary electron emission coefficient is set to $\gamma = 0.1$. Based on the simulation results, the time-averaged forces acting on dust particles, i.e. the ion drag force, F_i, electrostatic force, F_e and gravity, F_g, are calculated as a function of the position between the electrodes [40]. Here, the model of F_i provided by Barnes *et al* [61] is applied. F_e and F_g are simply expressed as $F_\mathrm{e} = Q_\mathrm{d}E$ and $F_\mathrm{g} = m_\mathrm{d}g$, where E and m_d are the time-averaged electric field and mass of dust particles, respectively. The charge of dust particles is calculated based on the standard formula: $Q_\mathrm{d} = 1400 r_\mathrm{d} T_\mathrm{e}$ for isolated dust particles, e.g. by Bonitz [21] or Piel [62], to be $Q_\mathrm{d} \approx -3300e$ in the plasma bulk (see figure 2), which is close to the typical value reported elsewhere [7]. Here e is the elementary charge. The typical error in the plasma bulk due to the spatial inhomogeneity is estimated to be about 10%. Finally, the spatial profiles of the potential energy are derived from the net forces exerted on dust particles.

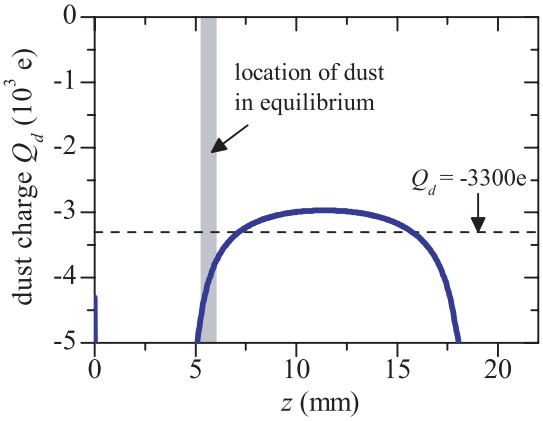

Figure 2. Estimated spatial profile of the dust charge based on the standard formula [21, 62] (Ar, 8 Pa, $\phi_0 = 200$ V, $\theta = 0°$). The dashed line shows the spatial average in the plasma bulk, that is used in this paper. The location of dust particles in equilibrium near the lower electrode, which is obtained experimentally, is also shown.

2.3. Analytical model of the RF sheath driven by an arbitrary voltage waveform

In this section a model of CCRF discharges is combined with the Child–Langmuir approximation to obtain the main properties of the RF sheath, i.e. the time-dependent sheath width and the spatio-temporal distribution of the potential and electric field inside the sheath, in an electrically asymmetric capacitive discharge. The goal is to calculate the time-averaged sheath electric field and correlate this field with the levitation of the dust particles above the powered electrode in the case of an adiabatic phase shift, discussed in section 3.2. The dynamics of the sheath in a 'classical' dual frequency discharge driven by two substantially different frequencies has been modelled using similar approaches [63–65]. According to the model, which has been introduced in [45, 66, 67], we find the following expression for the sheath voltage at the powered electrode normalized by ϕ_0

$$\bar{\phi}_\mathrm{sp}(t) = -\left[\frac{-\varepsilon q_\mathrm{t} + \sqrt{\varepsilon q_\mathrm{t}^2 - (1-\varepsilon)[\bar{\eta} + \bar{\phi}_\sim(t)]}}{1-\varepsilon}\right]^2. \quad (2)$$

Here ε, q_t, $\bar{\eta}$ and $\bar{\phi}_\sim(t)$ are the symmetry parameter as defined and discussed in [45], normalized total charge, the dc self-bias as well as the applied voltage normalized by ϕ_0, respectively. Equation (2) provides the sheath voltage as a function of time. In order to obtain a spatio-temporal model of the sheath electric field, the collisionless Child–Langmuir sheath theory [68] can be applied at low pressures of a few Pa. To simplify the analysis, we restrict ourselves to a one-dimensional scenario. In this approximation, the maximum width of the sheath adjacent to the powered electrode is expressed as $s_\mathrm{max,p} = \frac{\sqrt{2}}{3}\lambda_\mathrm{De}(2|\hat{\phi}_\mathrm{sp}|e/T_\mathrm{e})^{\frac{3}{4}}$, where $\hat{\phi}_\mathrm{sp}$, λ_De and T_e are the maximum of the sheath voltage at the powered electrode, the Debye length and the electron temperature at the sheath edge (in eV), respectively. The time-dependent sheath width is given by the scaling with the sheath voltage: $s_\mathrm{p}(t) = s_\mathrm{max,p}(\phi_\mathrm{sp}(t)/\hat{\phi}_\mathrm{sp})^{\frac{3}{4}}$. The minimum voltage drop across the powered sheath, $\hat{\phi}_\mathrm{sp} <$

0, is found from the voltage balance: $\phi_{\sim}(t)+\eta = \phi_{sp}+\phi_{sg}+\phi_b$ at the time of minimum applied voltage. Here ϕ_{sg} and ϕ_b are the sheath voltage at the grounded electrode and the bulk voltage, respectively. Neglecting the floating potential at the grounded sheath and ϕ_b yields $\hat{\phi}_{sp} \approx \tilde{\phi}_{min}+\eta$, so that the minimum sheath voltage can easily be deduced from experimentally measured values, for instance. Here $\tilde{\phi}_{min}$ is the minimum of the applied voltage. Assuming that both the electric field and the potential are zero at the sheath edge the spatio-temporal profile of the electric potential in the sheath region at the powered electrode ($0 \leqslant z \leqslant s_p(t)$) is expressed by [69]

$$\phi_{sp}(z,t) = -\frac{T_e}{2e}\left(\frac{3}{\sqrt{2}}\frac{s_p(t)-z}{\lambda_{De}}\right)^{\frac{4}{3}}. \quad (3)$$

Here $z = 0$ is the position of the powered electrode. Finally, the spatio-temporal profile of the electric field in the sheath region is found by differentiation:

$$E_{sp}(z,t) = -\frac{\partial\phi_{sp}(z)}{\partial z} = -\frac{\sqrt{2}T_e}{e\lambda_{De}}\left(\frac{3}{\sqrt{2}}\frac{s_p(t)-z}{\lambda_{De}}\right)^{\frac{1}{3}} \quad (4)$$

Equation (4) is used to understand the dust motion as a consequence of the adiabatic (continuous) phase change and to determine the electron density in section 3.2.

2.4. Model to describe the motion of dust particles

The motion of dust particles in plasmas is determined by the forces exerted on them [23, 61, 62, 70–72]. Here, we propose a simple analytical model to describe the one-dimensional transport of dust particles between both sheaths through the plasma bulk. Models of the dust motion based on the force balance have already been reported [18, 73–77]. We would like to emphasize again that the concentration of dust particles is quite low in this study and they do not disturb the plasma, which is different from the condition under which these models have been provided. Our approach focuses on analysing the particular dust transport which has been obtained experimentally when changing the phase angle abruptly, and in fact the model proposed here can explain the experimental results. Further studies are required to investigate non-Hamiltonian effects [78, 79] and clarify their role for the physics presented in this work. In reactors with horizontal plane parallel electrodes separated by a discharge gap, d, and in the absence of thermophoretic forces, negatively charged dust particles tend to be confined at the sheath edges, where the forces exerted on them balance. Right after introducing the dust particles into the discharge volume, they are typically located around the lower sheath edge due to gravity. Let us focus on the motion of dust particles between the sheath edge of the bottom (powered) electrode ($z = s_p$) and the upper (grounded) one ($z = d - s_g$), e.g. after applying an upward force at the lower equilibrium position. Later on, we will approximate the electrostatic force around the sheath edges as hard walls, i.e. the particles are instantaneously reflected without any change in their kinetic energy. This assumption is justified due to the fact that the electrostatic force caused by the bulk electric field (see figure 3) or the interaction between

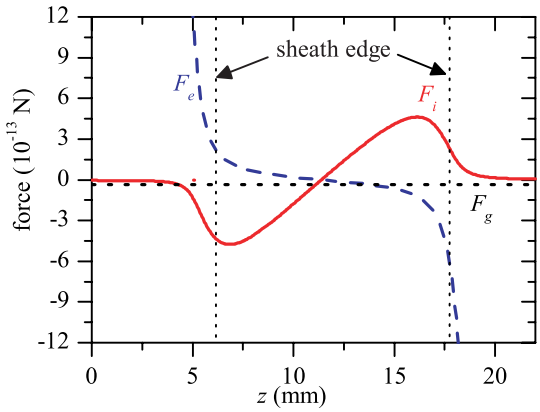

Figure 3. Spatial profile of electrostatic force, F_e, ion drag force, F_i, and gravity, F_g, exerted on dust particles. The spatial profile is obtained from PIC/MCC simulation (Ar, 8 Pa, $\phi_0 = 200$ V, $\theta = 0°$).

dust particles is negligible under our condition. One reason for this quite small bulk electrostatic force is the relatively high ion density in the bulk, which is also realized in the void formation in dusty plasmas [21, 23]. In contrast to our situation, the electrostatic force is of vital importance in complex plasmas, where the major contribution of negative charges to the total charge balance in the bulk is given by the dust particles and not by the electrons (see e.g., [18, 73, 80]). The inter-particle force, i.e. Coulomb force can be comparable to the sheath electrostatic force under certain conditions [81]. This becomes crucial particularly when the lateral motion of dust particles is discussed. This study is, however, focused only on their vertical motion. Additionally, dust particles are initially located only at the lower sheath edge due to the balance between the sheath electrostatic force and the ion drag force, suggesting that these two forces are dominantly exerted on the dust particles in this study. Thus, the vertical component of the Coulomb force is much smaller than the respective component of the sheath electrostatic force and the ion drag force. In our model, small errors occur only at the bulk side of the sheath edge (equilibrium position of dust particles) where the electrostatic force is neither close to zero nor represents a hard wall. The dust particles are assumed not to perturb the plasma. Within the plasma bulk region, the dust particle motion is associated with the following force balance:

$$m_d\ddot{z} = -m_d g - m_d\nu\dot{z} + F_i(z). \quad (5)$$

Here, m_d, g, ν, and F_i are the mass of a dust particle, the acceleration of gravity, the frequency of momentum loss due to collisions between dust particles and gas atoms [62, 82], and the ion drag force, respectively. Note that the gas friction force $m_d\nu\dot{z}$ is derived from the assumption that the velocity of dust particles is much smaller than the thermal velocity of gas molecules. Therefore, the dependence of ν on the particle velocity can be neglected. Any interaction between the dust particles, e.g. a repulsive Coulomb force [17–20, 80, 83], is not taken into account. Although the force profiles shown in figure 3 suggest that gravity can be neglected, we keep the corresponding term in the force balance to ensure the applicability of the resulting formulae for all types of particles, e.g. different sizes and/or mass densities (materials).

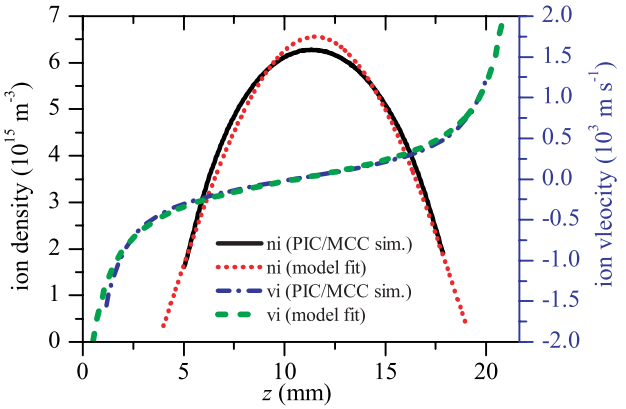

Figure 4. Spatial profile of ion density and velocity obtained from the PIC/MCC simulation and fit functions of the analytical model (Ar, 8 Pa, $\phi_0 = 200$ V, $\theta = 0°$).

There are several models of the ion drag force [61, 84, 85] and the analytical description of this force remains an interesting research topic in itself. There are discussions in the literature on the validity of the different models. Although more sophisticated models are available, the Barnes model [61] is applied here in order to calculate the ion drag force in a simple way. The formula is generally considered to be accurate at low dust densities as pointed out, e.g., in [23, 62], which is the case in this study. We assume that n_i as well as the ion velocity, v_i, are expressed by trigonometric functions, as it results from the basic diffusion estimation in a steady-state CCRF discharge [68]:

$$n_i(z) = n_{i0} \cos\left[\left(z - \frac{d}{2}\right)\frac{\pi}{\Lambda_i}\right], \tag{6}$$

$$v_i(z) = v_{i0} \tan\left[\left(z - \frac{d}{2}\right)\frac{\pi}{\Lambda_i}\right]. \tag{7}$$

Here, the maximum ion density, n_{i0}, and ion velocity, v_{i0}, are constants. Λ_i is the ion diffusion length; the value is actually close to the distance between the discharge centre and the sheath edges. These input parameters are determined by fitting to the PIC/MCC simulation data as shown in figure 4. The estimated model quantities from this fitting are $n_{i0} = 6.6 \times 10^{15}$ m^{-3}, $v_{i0} = 344$ m s^{-1}, $\Lambda_i = 15.5$ mm and $d = 23.0$ mm, respectively. The ion drag force consists of the collection force due to ions hitting the particle surface and the orbit force due to Coulomb collisions with the drifting ions. In low-pressure CCRF discharges the orbit force [61],

$$F_{i,\mathrm{orb}} = 4\pi n_i v_s m_i b_{\pi/2}^2 \Gamma, \tag{8}$$

typically dominates. Here, v_s, m_i, $b_{\pi/2}$ and Γ are the mean ion velocity, the ion mass, the impact parameter and the Coulomb logarithm [61], respectively:

$$b_{\pi/2} = \frac{eQ_d}{4\pi\epsilon_0 m_i v_s^2}, \tag{9}$$

$$\Gamma = \frac{1}{2}\ln\left(\frac{\lambda_{De}^2 + b_{\pi/2}^2}{r_d^2(1 - \frac{2e\phi_f}{m_i v_s^2}) + b_{\pi/2}^2}\right). \tag{10}$$

Note that these quantities depend on the radius (r_d), floating potential (ϕ_f) and charge (Q_d) of the dust particles. In this paper, we use the simplifying assumption of the dust particle charge to be negative and constant: $Q_d \approx -3300e$ as shown in figure 2.

In our approach, we neglect the thermal motion of the ions, i.e. the mean ion velocity v_s is given by the drift component, v_i:

$$v_s = \left(\frac{8k_B T_i}{\pi m_i} + v_i^2\right)^{\frac{1}{2}} \approx v_i. \tag{11}$$

Applying the approximation $F_i \approx F_{i,\mathrm{orb}} \propto n_i v_i$, the ion drag force becomes

$$F_i(z) = \bar{F}_{i0} \sin\left[\left(z - \frac{d}{2}\right)\frac{\pi}{\Lambda_i}\right]. \tag{12}$$

Here, the maximum ion drag force ($\bar{F}_{i0}$) is a constant. In order to solve equation (5) analytically only the linear variation of the sine function is considered here:

$$F_i(z) \approx F_{i0}\left(z - \frac{d}{2}\right)\frac{\pi}{\Lambda_i}, \tag{13}$$

with $F_{i0} = 4\pi m_i n_{i0} v_{i0} b_{\pi/2}^2 \Gamma$. The input parameters obtained from figure 4 provide $F_{i0} = 3.8 \times 10^{-13}$ N. Equation (13) corresponds to a strong simplification of $F_i(z)$ and deviations from the exact solution appear, particularly in the regions close to the sheath edges. However, our aim is to explain the transport of dust particles through the plasma bulk with this model. In the bulk region, the model is a reasonable approach, since it includes the most relevant forces in this region. Furthermore, the forthcoming analysis shows that the basic features of particle motion and the experimental observation of the dust transport can be explained reasonably well by this approach.

After inserting equation (13) into equation (5) a second order linear ordinary differential equation

$$m_d\ddot{z} + m_d\nu\dot{z} - F_{i0}\left[\left(z - \frac{d}{2}\right)\frac{\pi}{\Lambda_i}\right] + m_d g = 0 \tag{14}$$

needs to be solved. Note that equation (14) represents a harmonic oscillator in the space coordinate $(z - d/2)\pi/\Lambda_i$ with frequency $\sqrt{F_{i0}/m_d}$, which is externally driven by gravity and damped by collisions. Finally, using the boundary conditions $z(0) = z_0$ and $\dot{z}(0) = u_0$, which corresponds to the initial velocity of dust particles, the trajectory of dust particles is given by

$$z(t) = [\beta_1 \cosh(\alpha t) + \beta_2 \sinh(\alpha t)]\, e^{-\frac{\nu}{2}t} + \delta. \tag{15}$$

Here, α, β_1, β_2 and δ are:

$$\alpha = \sqrt{\left(\frac{\nu}{2}\right)^2 + \frac{\pi F_{i0}}{m_d \Lambda_i}}, \tag{16}$$

$$\beta_1 = x_0 - \frac{d}{2} - \frac{m_d \Lambda_i g}{\pi F_{i0}}, \tag{17}$$

$$\beta_2 = \left(u_0 + \beta_1 \frac{\nu}{2}\right) \alpha^{-1}, \tag{18}$$

$$\delta = \frac{m_\mathrm{d} \Lambda_\mathrm{i} g}{\pi F_{\mathrm{i}0}} + \frac{d}{2}. \tag{19}$$

From this trajectory of the dust particles, the kinetic energy is obtained

$$W(t) = \frac{1}{2} m_\mathrm{d} \dot{z}^2(t) = \frac{m_\mathrm{d}}{8\alpha^2} \left(-A\mathrm{e}^{\alpha t} + B\mathrm{e}^{-\alpha t}\right)^2 \mathrm{e}^{-\nu t}, \tag{20}$$

where A and B are defined as

$$A = g + \frac{F_{\mathrm{i}0}\pi d}{2 m_\mathrm{d} \Lambda_\mathrm{i}} - x_0 \frac{F_{\mathrm{i}0}\pi}{m_\mathrm{d} \Lambda_\mathrm{i}} + u_0 \left(\frac{\nu}{2} - \alpha\right), \tag{21}$$

$$B = g + \frac{F_{\mathrm{i}0}\pi d}{2 m_\mathrm{d} \Lambda_\mathrm{i}} - x_0 \frac{F_{\mathrm{i}0}\pi}{m_\mathrm{d} \Lambda_\mathrm{i}} + u_0 \left(\frac{\nu}{2} + \alpha\right). \tag{22}$$

Equation (20) is used to describe the dust energy as a consequence of the abrupt phase change in section 3.3. This rather complex result will be compared with the simple assumption that the kinetic energy of the dust particles is not affected by the particular shape of the potential profile and that the loss of the energy of the dust particles is only due to gas friction. Then, the velocity and kinetic energy of the dust particles can be estimated as

$$u_\mathrm{d}(t) = u_0 \mathrm{e}^{-\frac{\nu}{2}t}, \tag{23}$$

$$W(t) = \tfrac{1}{2} m_\mathrm{d} u_\mathrm{d}^2(t) = W_0 \mathrm{e}^{-\nu t}. \tag{24}$$

Here W_0 is the initial kinetic energy of dust particles. Equation (24) is used to determine the potential profile experimentally using the spatial profile of the laser light scattering (LLS) intensity from dust particles in section 3.3. It should be noted that practically the dust charge fluctuates and the reflection of the dust particles at the sheath edge is 'soft'. Again, our model aims to describe the dust transport observed in this study in a simple way, and thus the simple assumption, e.g. a constant dust charge and a rough approximation of the electrostatic force as a hard wall, is applied here.

3. Results and discussion

3.1. DC self-bias control via the EAE in a plasma containing a small amount of dust

Figure 5 shows the dc self-bias, η, obtained from the experiment, as a function of the phase angle, θ. η is generated as a monotonic function of θ. As described in detail before [45–47, 53, 55, 56, 67, 86], the EAE allows one to control the discharge symmetry electrically. The control range for gas pressures between 2 and 8 Pa and an applied voltage amplitude of $\phi_0 = 200$ V is found to be close to about 45% of the applied voltage amplitude. Therefore, a strong change in both the time-averaged sheath voltages ($\eta = \langle\phi_\mathrm{sp}(t)\rangle + \langle\phi_\mathrm{sg}(t)\rangle$) and the maximum sheath voltages as a function of θ can be expected. η is shifted towards negative values because the discharge setup becomes effectively geometrically asymmetric due to the parasitic effect of capacitive coupling between the glass cylinder and the grounded chamber walls [53, 87–91]. This

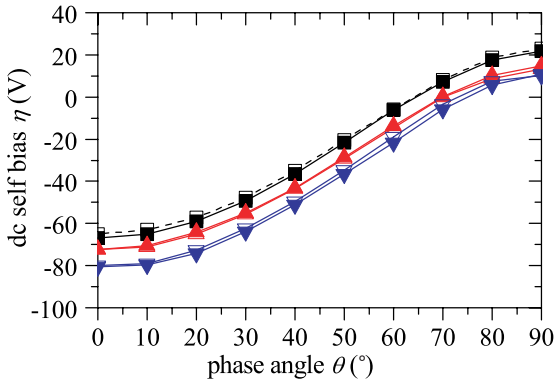

Figure 5. Experimentally obtained dc self-bias as a function of the phase angle θ with and without dust particles for different neutral gas pressures. The applied voltage amplitude is kept constant at $\phi_0 = 200$ V. Solid symbols relate to discharges without and open symbols to ones with dust particles. Square: 2 Pa, triangle: 4 Pa, inverted triangle: 8 Pa.

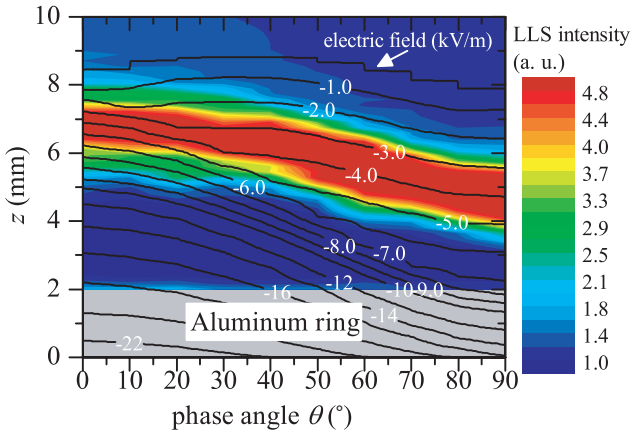

Figure 6. Spatial profile of the measured LLS intensity from the dust particles around the lower electrode as a function of the phase angle θ combined with the electric field calculated from the analytical model (Ar, 2 Pa, $\phi_0 = 200$ V). The observation of the LLS intensity within the lower region (0 mm $\leqslant z \leqslant$ 2 mm) is blocked by the aluminum ring.

effect tends to be stronger at higher pressures. It is important to note that in this study no significant difference of η in cases with and without dust particles is observed, indicating that the presence of a low dust concentration does not influence the plasma significantly. Therefore, the models described in the previous section are indeed applicable as pointed out already in section 1 by estimating Havnes' value P.

3.2. Adiabatic phase change

The dust particles injected into the discharge are initially located at the sheath edge adjacent to the lower electrode. Any adiabatic (continuous) change of θ leaves the dust particles at an equilibrium position close to this lower sheath edge as shown in figure 6. By increasing the phase angle from 0° to 90° adiabatically, the time-averaged sheath width becomes smaller and both the mean and the maximum sheath voltages at the lower electrode decrease. Therefore, the equilibrium position of the dust particles is shifted closer towards the electrode.

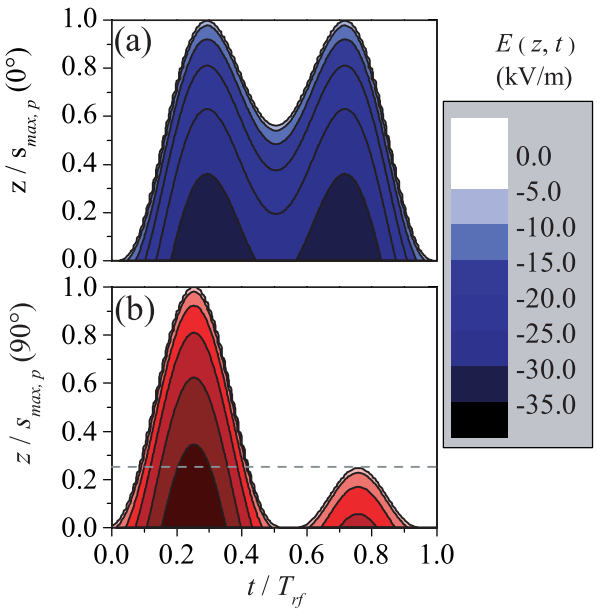

Figure 7. Distribution of the electric field at (*a*) $\theta = 0^\circ$ and (*b*) $\theta = 90^\circ$ as a function of spatial position within the phase angle-dependent maximum sheath width and time resulting from the model shown in equation (4) (Ar, 2 Pa, $\phi_0 = 200$ V). $T_{rf} = 74$ ns. The sheath reaches the region above dashed line only once per rf period.

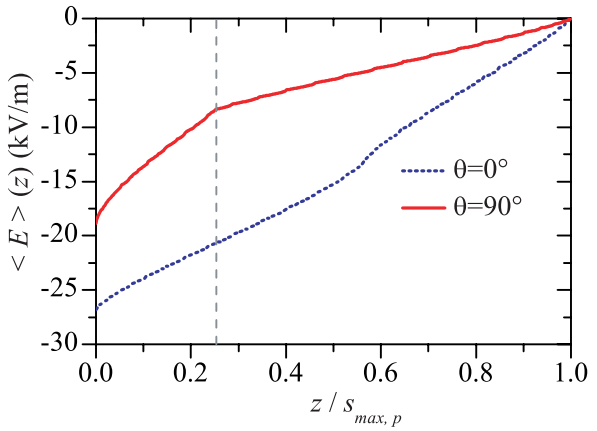

Figure 8. Strength of the time-averaged electric field as a function of position corresponding to figure 7. The dashed line is drawn according to that in figure 7(*b*). The gradient of the time averaged electric field changes at the boundary indicated by the dashed line.

This change of the equilibrium position can be understood by the electric field profile obtained from the analytical model described in section 2.3 using input parameters of $T_e = 3$ eV and $\lambda_{De} = 644\,\mu$m calculated under the assumption of $n_e = 4 \times 10^{14}\,\mathrm{m}^{-3}$ (see lines in figure 6). Electron density and temperature are taken from the PIC/MCC simulations because we applied a glass cylinder to confine the plasma. Thus, performing Langmuir probe measurements is not possible. We find very good agreement between the measured LLS and the part of the electric field distribution at a strength of about $-4\,\mathrm{kV\,m}^{-1}$, i.e. where forces exerted on dust particles balance. When θ is changed from 0° to 90°, the maximum of the time-averaged electric field in the powered electrode sheath, i.e. $\langle E \rangle_{\max}$ found at the electrode, becomes smaller due to the decrease in the mean sheath voltage. In addition, the change in the shape of the applied voltage as a function of θ leads to a change in the sheath voltage, $\phi_{sp}(t)$, which causes a change in the spatial distribution of the time-averaged electric field. As it becomes clear from figures 7 and 8, the slope of $\langle E \rangle(z)$ becomes flatter in the upper part of the sheath with increasing θ, i.e. the time-averaged voltage drop over this region becomes smaller. In particular, the field is relatively small during the second half of the rf period (see dashed line in figure 7(*b*)). Thus, the broadening of the equilibrium position (region of bright LLS) is well understood by the analytical model. This correlation analysis of the dust equilibrium position combined with the spatial electric field profile is applicable as a diagnostic tool to estimate plasma parameters, i.e. the dust particles can serve as electrostatic probes [38, 39, 92–94]. The correlation analysis yields the maximum sheath extension as the only free fitting parameter, which depends on electron temperature and density ($s_{\max,p} \propto \lambda_{De}/T_e^{3/4} \propto n_e^{-1/2} T_e^{-1/4}$). Hence, $s_{\max,p}$ is more sensitive to changes in the electron density and, if the electron temperature is known, n_e can be obtained assuming that these plasma parameters are constant, independently of θ. In our discharge configuration, it is not possible to measure T_e. However, estimating $T_e \approx 3$ eV, for instance, results in an electron density of about $n_e \approx 4 \times 10^{14}\,\mathrm{m}^{-3}$ at the sheath edge under the condition of figure 6 (Ar, 2 Pa and $\phi_0 = 200$ V). Note that the charge of dust particles becomes smaller than that in the plasma bulk when they are closer to the sheath edge as shown in figure 2, i.e. the charge of the dust particles observed in figure 8 might be smaller than $-3300e$ which is assumed as the dust charge in this paper. Further study is required to discuss this topic in detail.

3.3. Abrupt phase change

When the phase angle is changed abruptly from 90° to 0°, i.e. much faster than the reaction time scale of the particles, all dust particles are transported upwards into the plasma bulk and undergo rapid oscillations between the sheaths. Thereafter, a fraction of the particles reaches the upper sheath region and settles there (see figure 9(*a*)). In this way, sheath-to-sheath transport is realized [40]. Before discussing the conditions, under which sheath-to-sheath transport is possible, in more detail, this particle motion should be understood. As in the case of the adiabatic phase change, dust particles injected into the discharge are initially located at the sheath edge adjacent to the lower electrode. If the phase is changed abruptly from 90° to 0°, the dust particles are suddenly located in a region of high potential due to their inertia. Consequently, they bounce back and forth between both sheaths, while being decelerated by gas friction (see figure 10) [40]. As described in section 2.4, the motion of dust particles is determined by gravity, the ion drag force pushing the particles out of the bulk towards the sheaths, deceleration due to friction by collisions with the neutral gas, as well as electrostatic forces due to the sheath electric field, which basically can be regarded as boundaries, thus spatially confining the particle motion. Afterwards, they reside inside the potential well at either the upper or the lower sheath edge [40]. The shape of the potential profile consists

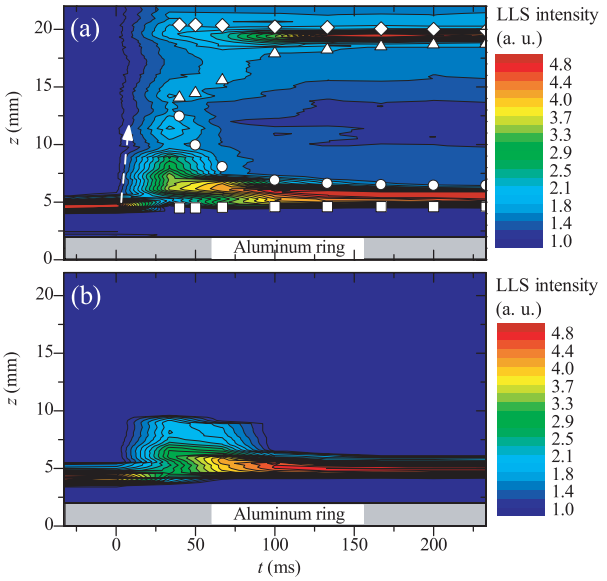

Figure 9. Spatiotemporal profiles of the measured LLS intensity by the dust particles within the discharge gap (Ar, (*a*) 8 Pa and (*b*) 12 Pa, $\phi_0 = 200$ V). The abrupt phase change takes place at $t \approx 0$ ms. Observation of the lower region (0 mm $\leqslant z \leqslant$ 2 mm) is blocked by the aluminum ring. The upper (diamond and triangle) and lower (circle and square) points are taken to obtain the upper and lower potential wells in figure 11, respectively. The arrow illustrates the estimation of an initail velocity of $u_0 \approx 1\,\mathrm{m\,s^{-1}}$.

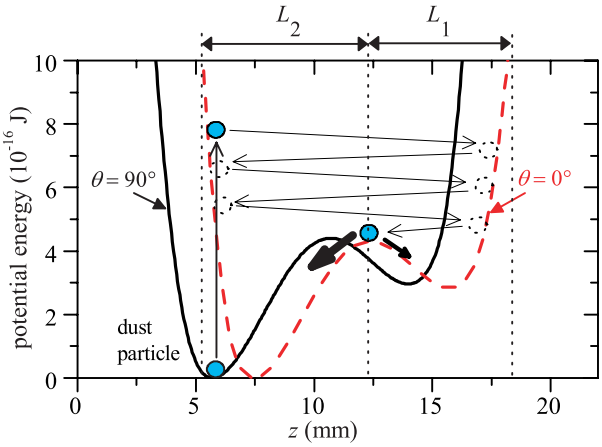

Figure 10. Model of sheath-to-sheath transport of dust particles [40]. The potential profile is calculated from PIC/MCC simulation data (Ar, 4 Pa, $\phi_0 = 200$ V). L_1 and L_2 are the widths of the upper and lower potential wells, respectively, at $\theta = 0°$.

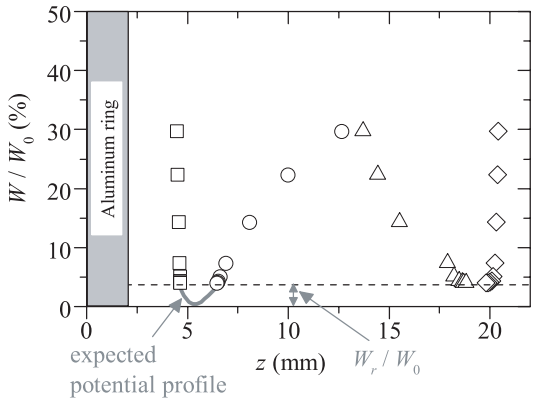

Figure 11. Potential profile at $\theta = 0°$ obtained from the measured 2DLLS intensity shown in figure 9(*a*) using a simple model. The potential energy scale is normalized by a rough estimation of the initial energy of the dust particles.

of a peak close to the discharge centre, two minima located around the sheath edges and steep rises inside the sheaths. The difference in the height of the two minima is mainly caused by gravity in the absence of thermophoretic forces. The term 'potential' is valid only, if the result does not depend on the particle velocity, i.e. if the time scale of the dust particle motion is the slowest of all time scales of interest here. This condition is fulfilled: for instance, the thermal motion of both the neutral and the ionized gas atoms is about two orders of magnitude faster compared with the dust particle motion (the maximum dust velocity estimated from the experimental results (figure 9) is a few $\mathrm{m\,s^{-1}}$ at most). Therefore, the potential profile is provided independently from the dust velocity.

It is possible to determine this potential distribution qualitatively from the experimental results. Hence, information on basic plasma properties might be achievable from this analysis. The shapes of the potential wells at the upper and lower sheath edges are obtained from the LLS profile (see four kinds of points in figure 9(*a*)). The points are taken at the contour line, which is both existent in the entire plasma bulk region and shows a reasonably high intensity. Note that the resulting data points are close to the region of maximum gradient of the LLS intensity, as well. The upper (diamond and triangle) and lower (circle and square) points correspond to the confinement regions of dust particles in the potential wells at the upper and lower sheath edges, respectively. In order to deduce the potential distribution from them, the temporal evolution of the energy of the dust particles needs to be known. The simplest model of the dust motion is applied here, i.e. dust particles lose their kinetic energy only due to gas friction. Using this approximation allows an analytical treatment of $W(t)$ using equation (24). Using the data points shown in figure 9(*a*) and replacing the time scale by the corresponding energy, the potential profile shown in figure 11 is obtained. Here, the potential energy scale is normalized by the initial energy of the dust particles. An estimation yields $W_0 \approx m_\mathrm{d} u_0^2/2 \approx 1.8 \times 10^{-15}$ J (11 keV) for an initial velocity of $u_0 \approx 1\,\mathrm{m\,s^{-1}}$, which was obtained from the spatiotemporal profile of the LLS intensity by the dust particles (see arrow in figure 9). Taking into account the uncertainty in W_0, we restrict ourselves to a qualitative discussion of the potential profile in this study. Comparing this profile with the one calculated from the simulation data shown in figure 12, we see that the position of the lower potential minimum agrees well between the experiment and the PIC simulation ($z \approx 5.7$ mm). In the experiment the upper minimum is located at 18.6 mm, whereas the position in the simulation is 16.9 mm. This difference is probably caused by the effective geometrical asymmetry of the discharge in the experiment, which is also indicated by the self-bias voltage, η (see the 8 Pa case in figure 5). In the PIC simulation the discharge is geometrically symmetric, thus yielding a symmetric dc self-bias curve ($\eta(\theta = 0°) = -\eta(\theta = 90°) \approx -52$ V) and a wider sheath compared with the

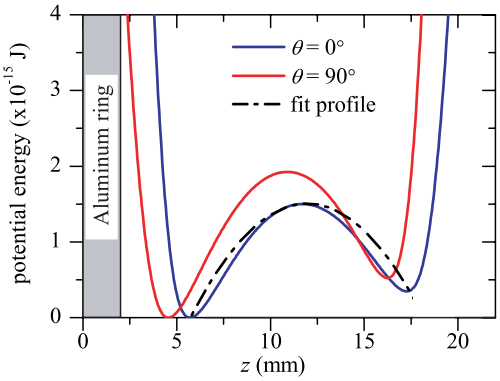

Figure 12. Potential profile calculated from PIC/MCC simulations data (Ar, 8 Pa, $\phi_0 = 200$ V). The model curve resulting from fits of equations (6) and (7) to PIC simulation data is shown, as well.

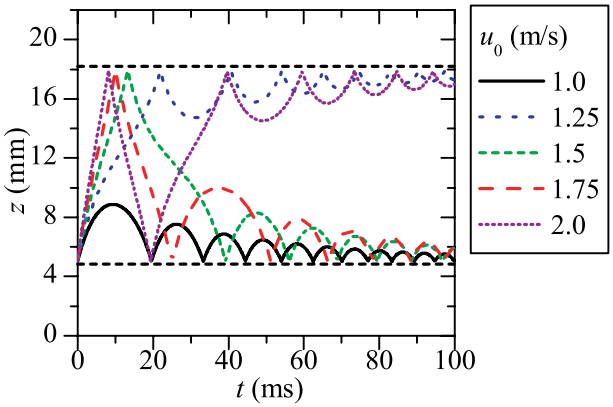

Figure 13. Trajectory of dust particles calculated from the model for different initial velocities (Ar, 8 Pa, $\phi_0 = 200$ V). The input parameter fitted on the data calculated from PIC/MCC simulations (see figure 12) are used.

Table 1. Summary of the effective transport of dust particles through the plasma bulk obtained in this study, depending on the initial velocity (Ar, 8 Pa, $\phi_0 = 200$ V). Odd number of N_{trans} realizes sheath-to-sheath transport, while even number of N_{trans} does not.

u_0 (m s^{-1})	1.00	1.25	1.5	1.75	2.0
N_{trans}	0	1	2	2	3

experiment at the grounded side for all θ. The lowest part of the potential curve resulting from the experimental data cannot be obtained by this approach (see the curve at around $z = 5$ mm in figure 11), since the residual spatial distribution is caused by the residual energy, W_r, of dust particles in equilibrium position due to thermal motion and Coulomb interaction, respectively, as well as the spatial resolution of the optical measurements (see the LLS intensity from dust particles after 100 ms in figure 9), which are neglected in our simple model. Except for this region, the dust particles can be used as probes to determine the potential, which depends on plasma properties via $F_{\text{i}}(z)$ and $F_{\text{e}}(z)$, in a major part of the discharge region. The probability for the trapping of dust particles at the upper sheath, P_{trans}, might be roughly estimated by the width of the upper potential well divided by the sum of the widths of the lower and upper potential wells, which is expressed as $L_1/(L_1 + L_2)$, in the simple approximation made above (see figure 10) [40]. Here L_1 and L_2 are the widths of the upper and lower potential wells, respectively. The probability calculated this way is about 0.5 for the experiment for 8 Pa and $\phi_0 = 200$ V, which agrees well with that calculated for the simulation potential profile.

Furthermore, the potential profile can be used to obtain input parameters for the analytical model of dust transport described in section 2.4. For this model the potential profile in the plasma bulk is obtained by integrating equation (14). Due to the small-angle approximation for the ion drag force (equation (13)) the potential profile is expressed by a simple parabola: $U(z) = U_0 - [F_{\text{i},0}(z - d)\frac{z\pi}{2\Lambda_{\text{i}}} - m_{\text{d}}gz]$, where U_0 is an integration constant. The model curve resulting from fits of equations (6) and (7) to PIC simulation data is shown in figure 12. One can find a difference of the central maxima of the potential profile obtained from PIC/MCC simulation for $\theta = 90°$ and $0°$. This is derived from the spatial profiles of the ion drag force (mainly orbit force), i.e. the direction of the ion drag force changes at the centre of the plasma bulk [40] and the gradient of the force profile for $\theta = 90°$ in this region is steeper than that for $\theta = 0°$, resulting in the difference of the central maxima for $\theta = 90°$ and $0°$. The model shows reasonable agreement with the potential profile using the exact values from the PIC/MCC simulation within the plasma bulk. As discussed above, deviations can be observed close to the sheath edges, e.g., due to the simplified treatment of the electrostatic force as a hard wall.

Figure 13 shows the trajectories of dust particles calculated from equation (15) and using the input parameters given above, for different values of the initial velocity. Right after the time of the abrupt phase shift all dust particles gain a certain initial velocity. If the initial velocity is below $u_0 \approx 1.0$ m s^{-1}, they cannot overcome the central maximum of the potential and bounce only inside the lower potential well. Dust particles with the initial velocity above $u_0 \approx 1.25$ m s^{-1} travel through the whole plasma bulk just after the phase shift. Dust particles with an initial velocity of $u_0 \approx 1.5$ m s^{-1} oscillate back and forth in the bulk region. However, their final equilibrium position is again located around the lower sheath. Therefore, from the model the initial velocity to realize the sheath-to-sheath transport is found at certain intervals, e.g. dust particles having $u_0 = 2.0$ m s^{-1} end up in the upper potential minimum while those having $u_0 = 1.75$ m s^{-1} do not. The conclusion obtained from figure 13 can be summarized by introducing the number of passages of dust particles through the plasma bulk, N_{trans}. Any odd number of N_{trans} means that sheath-to-sheath transport is realized, whereas even numbers of N_{trans} correspond to a final position close to the initial position at the lower sheath edge (table 1). We also note that the trajectory of $u_0 \approx 1.25$ m s^{-1} obtained from the model agrees well with the experimental result (figure 9(*a*)).

Using equation (20) the time evolution of the kinetic energy of the dust particles after the abrupt phase shift is obtained as shown in figure 14. An anharmonic oscillation is superimposed on the simple assumption of an exponential decay of the dust velocity (equation (24)) as a function of time. The sharp edges in this oscillations are due to the treatment of

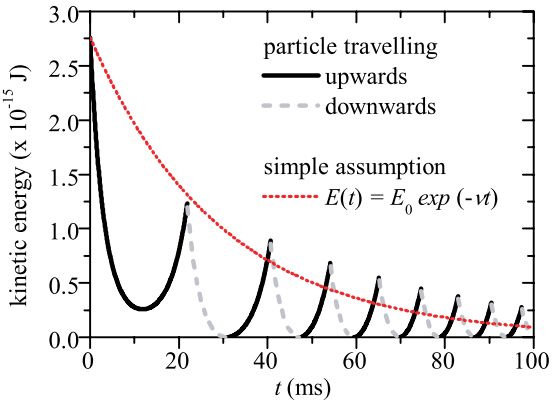

Figure 14. Time evolution of the kinetic energy of dust particles after the abrupt phase shift according to the $u_0 = 1.25\,\mathrm{m\,s^{-1}}$ case in figure 13 (Ar, 8 Pa, $\phi_0 = 200\,\mathrm{V}$).

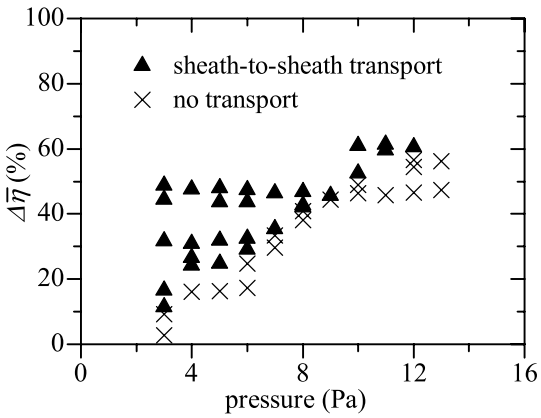

Figure 15. Experimentally obtained classification of the dust particle transport as a function of $\Delta\bar{\eta}$ and pressure. The voltage amplitude is kept at $\phi_0 = 200\,\mathrm{V}$ for $p < 10\,\mathrm{Pa}$ and $\phi_0 = 200$–$240\,\mathrm{V}$ for $p \geqslant 10\,\mathrm{Pa}$, respectively.

the electrostatic forces as hard walls. When the dust particles bounce between the sheath edges, they do not just lose their kinetic energy on long timescales, but they also gain kinetic energy temporarily due to the ion drag force while moving from the discharge centre towards the sheaths. However, the kinetic energy stays below $W_0 e^{-\nu t}$ between $t = 0$ and the time of trapping in one of the two potential wells. This is because the potential profile leads to a deceleration of the dust particles just after the abrupt phase change. Therefore, the dust particles spend even more time on their way to the upper sheath and undergo more collisions with the neutral gas, resulting in enhanced friction losses. The information on the trajectory and energy provided by the analytical model of dust transport is useful for the optimization of their transport: it can be understood that a monoenergetic initial distribution within one of the velocity intervals allowing sheath-to-sheath transport, e.g. $u_0 \approx 1.25\,\mathrm{m\,s^{-1}}$ in the case discussed here, is favourable to transport as many particles as possible to the upper sheath. Moreover, the outcome of the model suggests that the rough estimation of the probability of successful particle transport, P_{trans}, given above might overestimate the fraction of particles residing at the upper sheath edge, because the energy loss on the way from the upper sheath to the potential peak is much smaller than the energy loss occurring on the way from the lower sheath to the peak. In general, this model only requires the peak ion density at the discharge centre and the electron temperature as input parameters, which could be measured by other diagnostic methods. However, there is no simple access to apply such methods in our experimental setup. The upgrading of the experimental setup to obtain these key parameters is required for our further study.

3.4. Classification of transport conditions

We now turn to the discussion of conditions, under which sheath-to-sheath transport is possible. The key parameter for this transport is the rapid change of the dc self-bias, $\Delta\eta$, which can be easily controlled between $\Delta\eta_{\mathrm{min}} = 0$ and $\Delta\eta_{\mathrm{max}} = \eta(90^\circ) - \eta(0^\circ)$ by choosing certain intervals of the change in the phase angle (see figure 5). As shown in figure 15, a threshold value of $\Delta\bar{\eta}$ is apparently required to achieve the transport of a fraction of the particles to the upper equilibrium position. Here the difference of normalized dc self-bias $\Delta\bar{\eta}$ is given by $\Delta\bar{\eta} = [\eta(\theta_2) - \eta(\theta_1)]/\phi_0$ in the case of the phase shift from θ_1 to θ_2. The threshold increases with pressure, due to the increasing collisionality and, even more important, a stronger ion drag force, i.e. the central peak in the potential distribution becomes higher with increasing pressure. Therefore, it becomes more difficult for the particles to overcome this potential barrier. If $\Delta\bar{\eta}$ is smaller than the threshold, sheath-to-sheath transport is not realized: the dust particles reach a certain position below this potential peak and are forced towards the equilibrium position around the lower electrode sheath again (see figure 9(*b*)). In this case, similar to the adiabatic phase change, information on the local plasma properties might be gained from this disturbance of the particle distribution. In particular, we observe that the maximum displacement of the dust particles strongly depends on global parameters, such as pressure and voltage, in the experiment. However, a very good spatio-temporal resolution of the LLS measurements is required, which is not provided in our experiment. At low pressures, the sheath-to-sheath transport is possible within a wide range of $\Delta\bar{\eta}$ (see figure 15). However, as has been motivated by the model results shown in figure 13, the fraction of dust particles might vary as a function of $\Delta\bar{\eta}$. Figure 16 shows the normalized LLS intensity from dust particles around the upper sheath edge ($I_{\mathrm{upper}}/I_{\mathrm{all}}$) as a function of $\Delta\bar{\eta}$, for the abrupt phase shift. A low pressure of 4 Pa has been applied here. $I_{\mathrm{upper}}/I_{\mathrm{all}}$ is obtained by dividing the sum of the LLS intensity from dust particles around the upper sheath edge by that from dust particles around both sheath edges. The maximum of $I_{\mathrm{upper}}/I_{\mathrm{all}}$ is seen at $\Delta\bar{\eta} = 23\%$, and sheath-to-sheath transport is not achieved for $\Delta\bar{\eta} < 16\%$. These results indicate that the optimum initial velocity for sheath-to-sheath transport is slightly above the minimum value where sheath-to-sheath transport is realized. It also becomes clear that the change in the dc self-bias, $\Delta\bar{\eta}$, for the *efficient* sheath-to-sheath transport is found at a certain interval, e.g. dust particles are transported efficiently for $\bar{\eta} = 48\%$ and $\bar{\eta} = 23\%$, while they are not for $\bar{\eta} = 41\%$ (see figure 16). The initial velocity of dust particles, u_0, is controlled by

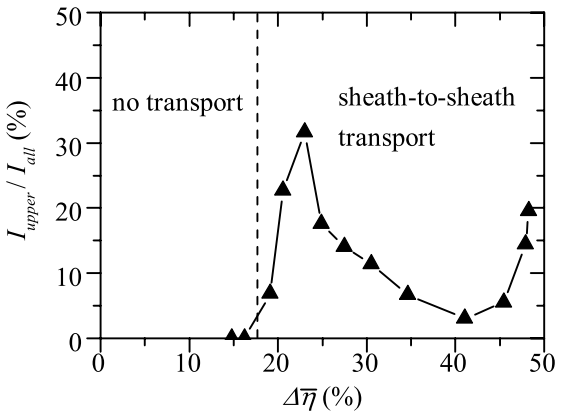

Figure 16. Normalized measured LLS intensity from dust particles around the upper sheath edge ($I_{\mathrm{upper}}/I_{\mathrm{all}}$) as a parameter of $\Delta\bar{\eta}$ for the abrupt phase shift (Ar, 4 Pa, $\phi_0 = 200$ V). $I_{\mathrm{upper}}/I_{\mathrm{all}}$ is obtained by dividing the sum of the LLS intensity from dust particles around the upper sheath edge by that from dust particles around both sheath edges.

changing $\Delta\bar{\eta}$, since the temporally averaged sheath voltage depends almost linearly on the dc self-bias [95] and it can be approximated that the initial energy of the dust particles is proportional to the change in the mean sheath voltage. Hence, $u_0 \propto \sqrt{\Delta\bar{\eta}}$ and these results support the model of the dust motion described above (figure 13).

4. Conclusion

The opportunities for controlling the transport of dust particles via the EAE have been discussed using the results of experiment, simulations, and analytical models. For these models, it has been confirmed that the dust particles do not significantly perturb the electrical properties of the discharge. In the case of an adiabatic tuning of the phase angle between the applied harmonics the dust particles are kept at an equilibrium position close to the lower sheath edge and their levitation is correlated with the time-averaged electric field profile. This might provide the opportunity to estimate the electron density using the dust particles as electrostatic probes. In the case of an abrupt phase shift ($90^\circ \rightarrow 0^\circ$) the dust particles are transported upwards, i.e. they move between both sheaths through the plasma bulk. The trajectory and the temporal evolution of the dust particle energy are well understood using an analytical model. It is found that an initial velocity of the dust particles of about 1.25 m s^{-1} is required to push them over the potential hill located around the centre of the plasma bulk. Thus, changing the applied voltage waveform via the EAE allows transporting a fraction of the dust particles from the equilibrium position around the lower sheath edge to the one at the upper electrode sheath, i.e. sheath-to-sheath transport is realized. The model also predicts that the initial velocity to realize sheath-to-sheath transport is found at certain intervals, which is in agreement with the dependence of the probability of sheath-to-sheath transport (fraction of LLS intensity at the upper sheath edge) on the change in the dc self-bias found in the experiment. Furthermore, a certain threshold value of the rapid change of the dc self-bias is required to achieve sheath-to-sheath transport. If the change in the dc self-bias lies below the threshold value, the dust particles move within the lower potential well. Due to an increase in the collisionality and in the height of the potential peak, the threshold increases and the displacement decreases as a function of neutral gas pressure.

Acknowledgments

This research was supported by the German Federal Ministry for the Environment (0325210B), the Alexander von Humboldt Foundation, the RUB Research Department Plasma, and the Hungarian Scientific Research Fund (OTKA-K-77653+IN-85261, K-105476, NN-103150).

References

[1] Fortov V E, Khrapak A G, Khrapak S A, Molotkov V I and Petrov O V 2004 *Phys. Usp.* **47** 447
[2] Fortov V E, Ivlev A V, Khrapak S A, Khrapak A G and Morfill G E 2005 *Phys. Rep.* **421** 1
[3] Nitter T 1996 *Plasma Sources Sci. Technol.* **5** 93
[4] Melzer A, Trottenberg T and Piel A 1994 *Phys. Lett.* A **191** 301
[5] Ivlev A V, Sütterlin R, Steinberg V, Zuzic M and Morfill G 2000 *Phys. Rev. Lett.* **85** 4060
[6] Hübner S and Melzer A 2009 *Phys. Rev. Lett.* **102** 215001
[7] Khrapak S A *et al* 2005 *Phys. Rev.* E **72** 016406
[8] Kalman G, Rosenberg M and DeWitt H E 2000 *Phys. Rev. Lett.* **84** 6030
[9] Nunomura S, Goree J, Hu S, Wang X and Bhattacharjee A 2002 *Phys. Rev.* E **65** 066402
[10] Couedel L, Mikikian M, Samarian A A and Boufendi L 2010 *Phys. Plasmas* **17** 083705
[11] Cavarroc M, Jouanny M C, Radouane K, Mikikian M and Boufendi L 2006 *J. Appl. Phys.* **99** 064301
[12] Hamaguchi S, Farouki R T and Dubin D H E 1997 *Phys. Rev.* E **56** 4671
[13] Melzer A, Homann A and Piel A 1996 *Phys. Rev.* E **53** 2757
[14] Meijer E J and Frenkel D 1991 *J. Chem. Phys.* **94** 2269
[15] Schweigert V A, Schweigert I V, Melzer A, Homann A and Piel A 1998 *Phys. Rev. Lett.* **80** 5345
[16] Aschinger A and Winter J 2012 *New J. Phys.* **14** 093036
[17] Thomas H, Morfill G E and Demmel V 1994 *Phys. Rev. Lett.* **73** 652
[18] Chu J H and I Lin 1994 *Phys. Rev. Lett.* **72** 4009
[19] Hayashi Y and Tachibana K 1994 *Japan. J. Appl. Phys.* **33** L804
[20] Arp O, Block D and Piel A 2004 *Phys. Rev. Lett.* **93** 165004
[21] Bonitz M, Henning C and Block D 2010 *Rep. Prog. Phys.* **73** 066501
[22] Shukla P K and Eliasson B 2009 *Rev. Mod. Phys.* **81** 25
[23] Bouchoule A 1999 *Dusty Plasmas* (Chichester: Wiley)
[24] Krasheninnikov S I and Soboleva T K 2005 *Plasma Phys. Control. Fusion* **47** A339
[25] Selwyn G S, Singh J and Bennett R S 1989 *J. Vac. Sci. Technol.* A **7** 2758
[26] Cavarroc M, Mikikian M, Tessier Y and Boufendi L 2008 *IEEE Trans. Plasma Sci.* **36** 1016
[27] Roca i Cabarrocas P, Nguyen-Tran Th, Djeridane Y, Abramov A, Johnson E and Patriarche G 2007 *J. Phys. D: Appl. Phys.* **40** 2258
[28] Shiratani M, Koga K, Iwashita S, Uchida G, Itagaki N and Kamataki K 2011 *J. Phys. D: Appl. Phys.* **44** 174038
[29] Koga K, Iwashita S and Shiratani M 2007 *J. Phys. D: Appl. Phys.* **40** 2267

[30] Wang X, Ocola L E, Divan R S and Sumant A V 2012 *Nanotechnology* **23** 075301
[31] Yan H, Choe H S, Nam S W, Hu Y, Das S, Klemic J F, Ellenbogen J C and Lieber C M 2011 *Nature* **470** 240
[32] Fumagalli F, Kylián O, Amato L, Hanůs J and Rossi F 2012 *J. Phys. D: Appl. Phys.* **45** 135203
[33] Kim H H, Ogata A, Schiorlin M, Marotta E and Paradisi C 2011 *Catal. Lett.* **141** 277
[34] Nosenko V, Goree J and Piel A 2006 *Phys. Plasmas* **13** 032106
[35] Nosenko V, Ivlev A V and Morfill G E 2010 *Phys. Plasmas* **17** 123705
[36] Piel A and Melzer A 2002 *Adv. Space Res.* **29** 1255
[37] Klindworth M, Melzer A, Piel A and Schweigert V A 2000 *Phys. Rev.* B **61** 8404
[38] Annaratone B M, Antonova T, Thomas H M and Morfill G E 2004 *Phys. Rev. Lett.* **93** 185001
[39] Beckers J, Ockenga T, Wolter M, Stoffels W W, van Dijk J, Kersten H and Kroesen G M W 2011 *Phys. Rev. Lett.* **106** 115002
[40] Iwashita S, Uchida G, Schulze J, Schüngel E, Hartmann P, Shiratani M, Donkó Z and Czarnetzki U 2012 *Plasma Sources Sci. Technol.* **21** 032001
[41] Samsonov D, Ivlev A V, Quinn R A, Morfill G and Zhdanov S 2002 *Phys. Rev. Lett.* **88** 095004
[42] Pustylnik M Y, Ohno N, Takamura S and Smirnov R 2006 *Phys. Rev.* E **74** 046402
[43] Knapek C A, Samsonov D, Zhdanov S, Konopka U and Morfill G E 2007 *Phys. Rev. Lett.* **98** 015004
[44] Pustylnik M Y, Ivlev A V, Thomas H M, Morfill G E, Vasilyak L M, Vetchinin S P, Polyakov D N and Fortov V E 2009 *Phys. Plasmas* **16** 113705
[45] Heil B G, Czarnetzki U, Brinkmann R P and Mussenbrock T 2008 *J. Phys. D: Appl. Phys.* **41** 165202
[46] Schulze J, Schüngel E, Donkó Z and Czarnetzki U 2009 *J. Appl. Phys.* **106** 063307
[47] Schulze J, Schüngel E, Donkó Z and Czarnetzki U 2011 *Plasma Sources Sci. Technol.* **20** 015017
[48] Lafleur T and Booth J P 2012 *J. Phys. D: Appl. Phys.* **45** 395203
[49] Boufendi L, Jouanny M Ch, Kovacevic E, Berndt J and Mikikian M 2011 *J. Phys. D: Appl. Phys.* **44** 174035
[50] Watanabe Y, Shiratani M, Fukuzawa T and Kawasaki H 1994 *Plasma Sources Sci. Technol.* **3** 355
[51] Schüngel E, Mohr S, Iwashita S, Schulze J and Czarnetzki U 2013 *J. Phys. D: Appl. Phys.* **46** 175205
[52] Havnes O, Aanesen T K and Melandso F 1990 *J. Geophys. Res.* **95** 6581
[53] Schulze J, Schüngel E and Czarnetzki U 2009 *J. Phys. D: Appl. Phys.* **42** 092005
[54] Xu R 2002 *Particle Characterization: Light Schattering Methods* (Dordrecht: Kluwer)
[55] Donkó Z, Schulze J, Heil B G and Czarnetzki U 2009 *J. Phys. D: Appl. Phys.* **42** 025205
[56] Donkó Z, Schulze J, Czarnetzki U and Luggenhölscher D 2009 *Appl. Phys. Lett.* **94** 131501
[57] Donkó Z 2011 *Plasma Sources Sci. Technol.* **20** 024001
[58] Choi J S, Ventzew P L G, Hoekstra R J and Kushner M J 1994 *Plasma Sources Sci. Technol.* **3** 419
[59] Schweigert I V, Alexandrov A L, Ariskin D A, Peeters F M, Stefanović V, Kovačević E, Berndt J and Winter J 2008 *Phys. Rev.* E **78** 026410
[60] Matyash K, Schneider R, Taccogna F, Hatayama A, Longo S, Capitelli M, Tskhakaya D and Bronold F X 2007 *Contrib. Plasma Phys.* **47** 595
[61] Barnes M S, Keller J H, Forster J C, O'Neill J A and Coultas D K 1992 *Phys. Rev. Lett.* **68** 313
[62] Piel A 2010 *Plasma Physics* (Berlin: Springer)
[63] Robiche J, Boyle P C, Turner M M and Ellingboe A R 2003 *J. Phys. D: Appl. Phys.* **36** 1810
[64] Franklin R N 2003 *J. Phys. D: Appl. Phys.* **36** 2660
[65] Jiang W, Mao M and Wang Y N 2006 *Phys. Plasmas* **13** 113502
[66] Schulze J, Heil B G, Luggenhölscher D, Brinkmann R P and Czarnetzki U 2008 *J. Phys. D: Appl. Phys.* **41** 195212
[67] Czarnetzki U, Schulze J, Schüngel E and Donkó Z 2011 *Plasma Sources Sci. Technol.* **20** 024010
[68] Lieberman M A and Lichtenberg A J 2005 *Principles of Plasma Discharges and Materials Processing 2nd edn* (Hoboken, NJ: Wiley)
[69] Oksuz L and Hershkowitz N 2005 *Plasma Sources. Sci. Technol.* **14** 201
[70] Garrity M P, Peterson T W, Garrett L M and O'Hanlon J F 1995 *J. Vac. Sci. Technol.* A **13** 2939
[71] Rothermel H, Hagl T, Morfill G E, Thoma M H and Thomas H M 2002 *Phys. Rev. Lett.* **89** 175001
[72] Liu B, Goree J, Fortov V E, Lipaev A, Molotkov V I, Petrov O F, Morfill G E, Thomas H M and Ivlev A V 2010 *Phys. Plasmas* **17** 053701
[73] Couëdel L, Nosenko V, Zhdanov S K, Ivlev I V, Thomas H M and Morfill G E 2009 *Phys. Rev. Lett.* **103** 215001
[74] Nefedov A P *et al* 2003 *New J. Phys.* **5** 33
[75] Land V and Goedheer W J 2007 *New J. Phys.* **9** 246
[76] Zhakhovski V V, Molotkov V I, Nefedov A P, Torchinski V M, Khrapak A G and Fortov V E 1997 *JETP Lett.* **66** 419
[77] Graves D B, Daugherty J E, Kilgore M D and Porteous R K 1994 *Plasma Sources Sci. Technol.* **3** 433
[78] Tuckerman M E, Mundy C J and Martyna G J 1999 *Europhys. Lett.* **45** 149
[79] Kompaneets R, Vladimirov S V, Ivlev A V, Tsytovich V and Morfill G 2006 *Phys. Plasmas* **13** 072104
[80] Takahashi K, Oishi T, Shimomai K, Hayashi Y, and Nishino S 1998 *Phys. Rev.* E **58** 7805
[81] Hwang H H and Kushner M 1997 *J. Appl. Phys.* **82** 2106
[82] Epstein P S 1924 *Phys. Rev.* **23** 710
[83] Chu J H, Du J-B and Lin I 1994 *J. Phys. D: Appl. Phys.* **27** 296
[84] Khrapak S A, Ivlev A V, Morfill G E and Zhdanov S K 2003 *Phys. Rev. Lett.* **90** 225002
[85] Fortov V E and Morfill G E 2009 *Complex and Dusty Plasmas* (Boca Raton, FL: CRC Press)
[86] Schüngel E, Zhang Q Z, Iwashita S, Schulze J, Hou L J, Wang Y N and Czarnetzki U 2011 *J. Phys. D: Appl. Phys.* **44** 285205
[87] Coburn J W and Kay E 1972 *J. Appl. Phys.* **43** 4965
[88] Lieberman M A and Savas S E 1990 *J. Vac. Sci. Technol.* A **8** 1632
[89] Johnson E V, Verbeke T, Vanel J C and Booth J P 2010 *J. Phys. D: Appl. Phys.* **43** 412001
[90] Johnson E V, Delattre P A and Booth J P 2012 *Appl. Phys. Lett.* **100** 133504
[91] Lafleur T, Boswell R W and Booth J P 2012 *Appl. Phys. Lett.* **100** 194101
[92] Basner R, Sigeneger F, Loffhagen D, Schubert G, Fehske H and Kersten H 2009 *New J. Phys.* **11** 013041
[93] Schubert G, Basner R, Kersten H and Fehske H 2011 *Eur. Phys. J.* D **63** 431
[94] Maurer H R, Schneider V, Wolter M, Basner R, Trottenberg T and Kersten H 2011 *Contrib. Plasma Phys.* **51** 218
[95] Schüngel E, Schulze J, Donkó Z and Czarnetzki U 2011 *Phys. Plasmas* **18** 013503